pp 735–756. © Royal Aeronautical Society 2016
doi: 10.1017/aer.2016.29

Experimental investigation of flowfield over an iced aerofoil

M.D. Manshadi
mdmanshadi@alum.sharif.edu
Department of Mechanical and Aerospace Engineering
Malekashter University of Technology
Isfahan
Iran

M.K. Esfeh
School of Mechanical Engineering
Yazd University
Yazd
Iran

ABSTRACT

Wind-tunnel measurements were used to study the characteristics of the unsteady separation bubbles on a NACA 0015 aerofoil with simulated two-dimensional leading-edge glaze ice accretions. The unsteadiness present in the iced-aerofoil flowfield was determined using measurements of the time-dependent aerofoil surface pressure distribution at Reynolds number of 1.0×10^6. Additionally, the unsteady flow features were investigated through the power spectrum of the stream-wise velocity fluctuations using a hot-wire anemometry. The results showed that the highest value of root-mean-square fluctuation of the surface pressure consistently occurred upstream of the mean shear-layer reattachment location. Spectral analysis of stream-wise velocity fluctuations near reattachment location revealed evidence of the regular frequency at Strouhal numbers of 0.5-0.63. Moreover, the low-frequency oscillations associated with shear-layer flapping was also identified in the wake velocity spectra on the order of 10 Hz that resulted in Strouhal numbers of 0.0186-021.

Keywords: iced-aerofoil; unsteady separation bubbles; pressure distribution; hot-wire anemometry

Received 13 March 2015; revised 11 November 2015; accepted 11 December 2015.

NOMENCLATURE

c	aerofoil chord length
C_p	pressure coefficient
$C_{p,i}$	instantaneous pressure coefficient
C'_p	root mean square of the unsteady pressure coefficient
f	frequency
k	protuberance height
L_b	bubble length
L_h	projected height (normal to freestream)
N	number of samples
Re	Reynolds number based on chord length
RMS	root mean square
s	model/aerofoil coordinate in surface length
St_f	Strouhal number corresponding to shear-layer flapping
St_r	Strouhal number corresponding to regular mode
V	freestream velocity
x	coordinate in the aerofoil model chord-wise direction
x_{MR}	mean reattachment location
w	protuberance base width
α	aerofoil angle-of-attack
θ	ice shape horn angle with respect to the chord line

1.0 INTRODUCTION

Determining the aerodynamic effects of ice accretion on aircraft surfaces is an important step in flight safety. Reductions in aerofoil maximum lift of over 50% and increases in minimum drag of more than 400% have been observed for some types of ice accretion[1,2]. It can also severely alter the stability and control characteristics of the aircraft. When an aircraft enters a region containing super-cooled water droplets, ice accretions of various shapes can form at different locations on its aerodynamic surfaces under different meteorological and flight conditions. The three primary ice shapes encountered are rime ice, glaze ice and ridge ice. Glaze ice (with a more irregular ice shape) forms at temperatures near freezing when some of the water droplets partly freeze on impact and the rest run back. This often results in the development of a horn-ice shape. Glaze ice accretions tend to be studied more than any other type of shape because of the large aerodynamic penalties. Glaze ice accretion dangerously affects and alters the shape of the original wing surface, producing aerodynamic penalties much more severe than ice roughness, rime ice and short ridge ice. For this reason, the present study has focused on glaze ice accretion.

As discussed by Bragg et al[3], the most dominant feature in the flowfield of an aerofoil with a horn-ice shape is the large separation bubble that forms due to the separation off the tip of the horn-ice shape. An instantaneous schematic of the horn-ice induced flowfield, including the ice-induced separation bubble and associated flowfield features, is shown in Fig. 1, after Gurbacki and Bragg[4]. Air flows around the upper horn of the ice shape and separates due to a severe adverse pressure gradient. Shear-layer vortices enhance flow mixing, which leads to reattachment and the creation of a separation bubble[4]. At higher angles of attack, the pressure recovery may not be achieved and stall may occur. Due to flow unsteadiness, the reattachment location on the aerofoil surface varies in time, forming a reattachment zone[4].

https://doi.org/10.1017/aer.2016.29 Published online by Cambridge University Press

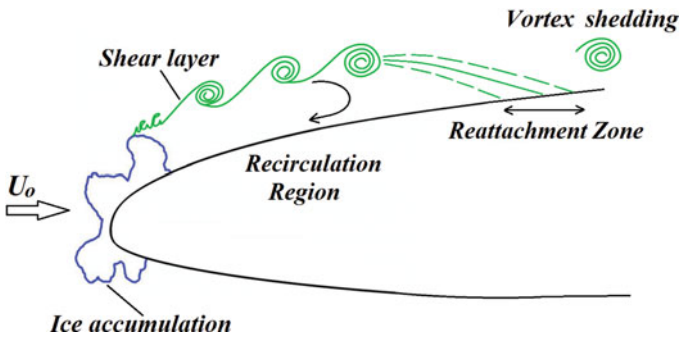

Figure 1. (Colour online) Instantaneous schematic of the flowfield downstream of a horn-ice shape, after Gurbacki and Bragg[4].

The behaviour of large-scale vortex shedding and the differences in the iced-aerofoil flowfields between a three-dimensional ice shape casting and a two-dimensional extrusion of the ice shape casting were identified by Jacobs and Bragg[5,6]. From this investigation, it was discovered that the three-dimensional horn-ice shape produced stream-wise vortex structures, which led to a faster pressure recovery of the separated boundary layer, and thus a shorter mean reattachment length than the two-dimensional extrusion of the ice shape.

Accurate prediction of aerofoil performance penalties rests partially on the ability to correctly predict the unsteady flowfield characteristics associated with the ice-induced separation bubble[4]. Gurbacki and Bragg[4] identified two primary sources of ice-induced unsteadiness for an aerofoil with leading-edge horn-ice shapes.

The first source has been attributed to vortical motion, where large-scale vortices are regularly shed downstream of the separation bubble according to a bandwidth of frequencies. The source of the regular mode has almost unanimously been attributed to the Kelvin-Helmholtz instability, where the difference between the velocity within the recirculation region of the separation bubble and the external flow causes a roll-up and shedding of vortices in the shear layer[7-9].

The unsteady content of the iced-aerofoil flowfield was analysed by Gurbacki and Bragg[4] for a NACA 0012 aerofoil with a leading-edge horn-ice shape. Power spectra of time-dependent surface pressure data near reattachment presented unsteadiness with non-dimensional frequency St = 0.53-0.73. These frequencies corresponded to shear-layer vortices and vortex shedding from the separation bubble. In a joint experimental wind-tunnel and Computational Fluid Dynamics (CFD) simulation, Mirzaei et al[10] investigated the flowfield structure of the separation bubble formed on NLF-0414 aerofoil with glaze ice accretions. Measurements of the unsteadiness of the flowfield near reattachment location confirmed the existence of the vortices in the shear-layer with the non-dimensional frequency ranging from 0.44 to 0.78.

The flow structures downstream of horn-ice shapes have many similarities to the unsteady flowfield behaviour downstream of a backward-facing step or a blunt flat plate[4]. Cherry et al[11] studied the unsteady structure of the 2D separation bubble present on a blunt flat plate using a combination of pressure and velocity measurements, along with flow visualisation. They observed vortex shedding at a Strouhal number of 0.7 from shear-layer velocity fluctuations. Driver et al[12] observed the maximum energy in the instantaneous pressure near reattachment of the backward-facing step's shear-layer at a Strouhal number of 0.6. For the same geometry, Eaton and Johnston[13] identified a value of 0.52 from the power spectrum

https://doi.org/10.1017/aer.2016.29 Published online by Cambridge University Press

of the stream-wise velocity fluctuations near reattachment. Kiya and Sasaki[14] studied the large-scale vortex structure of the separation bubble across the surface of a blunt flat plate using unsteady velocity and surface pressure measurements. They observed a regular, periodic shedding of vortices with dimensionless frequency of 0.6.

The second source of unsteadiness is represented by a low-frequency 'flapping' of the shear layer, which causes large-scale unsteadiness in the separation bubble flowfield and a quasi-periodic enlargement and shrinking of the separation bubble. The source of this low-frequency flapping of the shear layer is not fully understood. Kiya et al[15] have theorised the existence of a feedback system that drives this low-frequency oscillation. This theory was later reinforced by the observations of Lee and Sung[16], who identified traits in the unsteady pressure that were characteristic of a standing wave at the shear-layer flapping frequency inside the separation bubble region. Sigurdson[17] attributed this low-frequency flapping to a parallel version of a von Kármán vortex shedding process, where an instability is generated due to the interaction of the shear-layer vorticity with its image across a wall. Eaton and Johnston[13] believe that the low-frequency unsteadiness in the shear-layer reattachment is due to an instantaneous imbalance between shear layer entrainment from the re-circulating region on one hand and reinjection of fluid near the reattachment on the other hand.

The low-frequency oscillation on iced-aerofoils was first pursued in great detail by Zaman and Potapczuk[18], who characterised the low-frequency oscillations using computational methods and hot-wire data. These authors identified oscillations in the wake of a NACA 0012 aerofoil with a leading-edge ice accretion at Strouhal numbers (based on projected aerofoil height) near 0.02. Bragg et al[3] also identified a low-frequency oscillation in the split-film measurements acquired in the shear layer downstream of a horn-ice shape on a NACA 0012 aerofoil. A peak in the spectral content of the velocity in the shear layer at $\alpha = 4°$ revealed a low-frequency oscillation at 11.6 Hz. This frequency corresponded to a Strouhal number of 0.0185, which was similar to the Strouhal number reported in the experimental portion of Zaman and Potapczuk[18]. In most simple-geometry flowfields, shear-layer flapping has been observed to be associated with Strouhal numbers on the order of 0.02 based on the height of the geometric feature and the freestream velocity, or on the order of 0.1 based on the mean length of the separation bubble and the freestream velocity[11,12].

Almost all previous studies are focused on the effect of ice accretion with a fixed configuration on aerofoil aerodynamics[3-6,10]. Because the ice accretion process is dependent on both atmospheric and aerodynamic conditions, the ice shape with many different sizes, shapes, locations and textures is formed on unprotected aerodynamic surfaces. Therefore, more investigation with a wide range of varying ice shapes is required to acquire more insight into the flowfield characteristics of aerofoils under icing conditions. In the present work, for the first time the effect of height and location of ice accretion on the flowfield unsteadiness of the separation bubble formed on a NACA 0015 aerofoil has been investigated using time-dependent pressure measurements. Moreover, an attempt is made to characterise relevant modes of unsteadiness present in the iced-aerofoil flowfield by spectral analysis of stream-wise velocity fluctuations using a hot-wire anemometry.

2.0 EXPERIMENTAL SET-UP

Flow measurements were carried out by using an open return wind tunnel with a test section height, width and length of 90, 90 and 2,000 cm, respectively. The maximum empty test section speed of this wind tunnel is approximately 70 m/s, resulting in a maximum Reynolds

https://doi.org/10.1017/aer.2016.29 Published online by Cambridge University Press

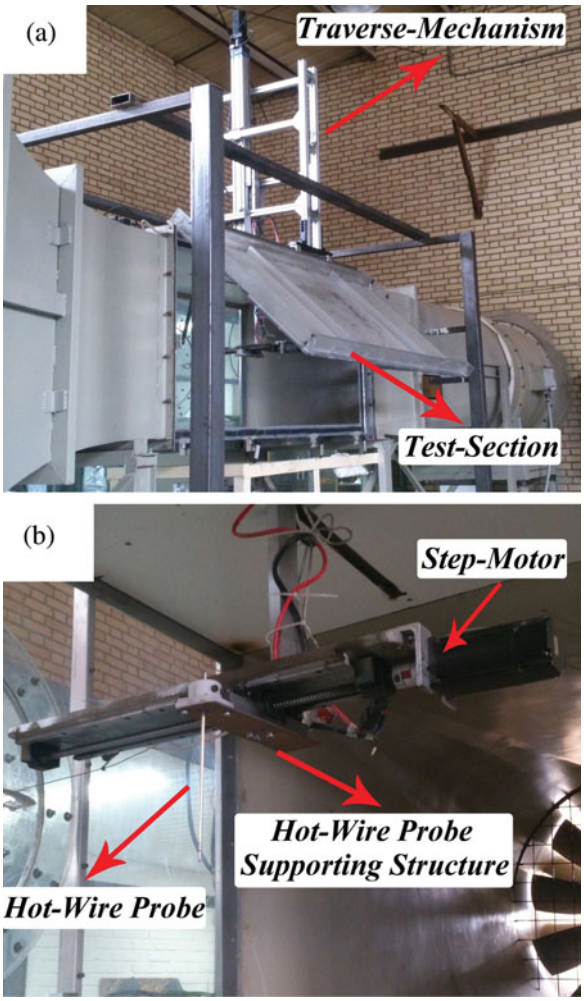

Figure 2. (Colour online) Wind-tunnel set-up: (a) traverse mechanism, (b) flowfield measurements apparatus installed in the test section.

number of 1.5×10^6/m. The contraction ratio between the settling chamber and test section is 7.5:1 and a honeycomb and three turbulence reduction screens are located at the inlet settling chamber to reduce tunnel turbulence to less than 0.2% in the test section. The flowfield measurements require some equipment both inside and outside the test section. The wind-tunnel test section is equipped with a three-axis traverse system, which can be controlled by a LabVIEW computer program (Fig. 2(a)). This traverse system is mounted above the wind tunnel such that the hot-wire probe supporting structure enters the wind tunnel from the ceiling as shown in Fig. 2(b). Three step-motors are used in the traversing mechanism to control the vertical and horizontal position of the measurement probe of the hot-wire system with the accuracy of ± 0.1 mm.

The aerofoil model used for this investigation is aluminium NACA 0015 with a 38 cm chord and 90 cm span. The upper surface of aerofoil was instrumented with 27 surface pressure taps for acquiring pressure measurements (Fig. 3(a)). All pressure taps are connected to a pressure

https://doi.org/10.1017/aer.2016.29 Published online by Cambridge University Press

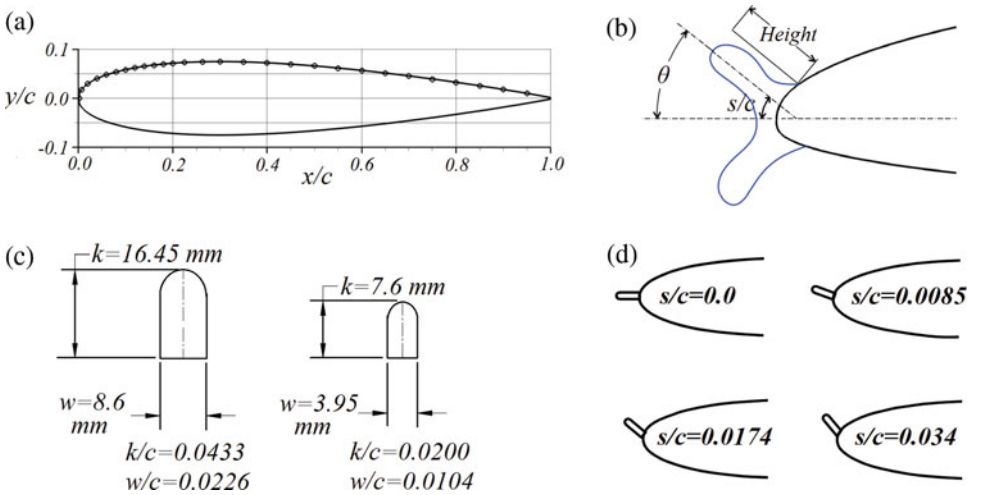

Figure 3. (Colour online) (a) Positions of the surface pressure taps, (b) geometry of a horn-ice shape, (c) glaze horn-ice simulations, (d) surface locations of simulated ice shape.

box. For this purpose, the PU plastic tubes with an inside diameter of 1.5 mm and length of 120 cm are employed. It should be pointed out that since the trailing edge is too thin, no pressure taps are installed for $x/c > 0.90$. In this investigation, all data are obtained at a chord-based Reynolds number of 1.0×10^6.

As discussed by Bragg et al[19] the glaze ice shape can be characterised by its height, the angle it makes with respect to the chord line (θ) and its location indicated by s/c, the non-dimensional surface length (Fig. 3(b)). In this investigation, the simulated glaze horn-type ice accretions were determined from averaging geometry data from a set of actual ice accretions collected in a test at the NASA Glenn Icing Research tunnel[20]. Leading-edge glaze ice accretions characteristically consist of an upper and lower surface horn. However, only single-horn simulations were used for this research. The simulated ice shapes were machined to the designed shape geometry from a solid aluminium bar to produce adequate shape accuracy. The simulated ice was tested in two heights: $k = 7.6$ ($k/c = 0.02$) and $k = 16.45$ ($k/c = 0.0433$) mm (Fig. 3(c)). Each of these shapes was positioned at four locations around the leading edge of aerofoil. Figure 3(d) shows the locations (s/c) of simulated ice shapes. Lee and Bragg[21] showed that the horn radius had only a small effect on the aerofoil performance, so varying the glaze-ice horn leading-edge radius is ignored in the current study.

Surface pressure was sensed through ASDX series transducers, from Honeywell, with an accuracy of ±2% full-scale output and 1 kHz sample rate frequency. An estimate of the unsteady content present in the iced-aerofoil flowfield was determined by calculating the root mean square of the un-steady pressure coefficient, which was calculated by utilising the following relation:

$$C'_p = \left(\frac{1}{N-1} \sum_{1}^{N} \left(C_{p,i} - C_p \right)^2 \right)^{0.5}, \qquad \ldots (1)$$

where N represents the number of instantaneous pressure samples acquired. In this equation, C_p and $C_{p,i}$ are the time-averaged pressure coefficient and the instantaneous pressure

https://doi.org/10.1017/aer.2016.29 Published online by Cambridge University Press

coefficient, respectively. Surface pressure coefficient fluctuations were acquired at 1,000 Hz for 10 sec. In unsteady measurements where the pressure changes with time continuously, it is important to determine the time lag of pressure-measuring system when the transducers are not installed inside the model. The time lag in the tubing is due to the viscosity, elasticity, mass of the air enclosed in the tube, inertia, material of which the tube is made and the condition of the inside surface of the tube. The lag due to the viscosity and elasticity of the air depends chiefly on the length and diameter of the tube and the time rate of change of the initial pressure[22,23]. All of the tubes that were used in this investigation have the same length and diameter. Based on Soltani's[24] results, the time lag of the tubes used in this study is about 0.005 sec. The uncertainties in relative time-average and time-dependent pressure measurements were obtained as 2.4% and 3.8%, respectively.

The turbulence intensity and spectral analysis data were measured using a single hot-wire probe. The probe was calibrated both statically and dynamically and all data were low-pass filtered. Data were recorded via a 12-bit A/D. In order to quantify the uncertainty of the hot-wire anemometer, the methodology provided in Refs 25 and 26 were followed. The uncertainty of the results obtained with the CTA anemometer is a combination of the uncertainties of the individually acquired voltages converted into velocity. The uncertainty of each individual velocity sample was determined by non-statistical means based on detailed knowledge about the instrumentation, calibration equipment and experimental conditions. The hot-wire anemometer has low drift, low noise and good repeatability, so that these factors do not add significantly to the uncertainty in comparison with other error sources[25]. Temperature variations from calibration to experiment or during an experiment introduce systematic errors. Because of this, every CTA is equipped with a temperature corrective probe that is placed in the flow and applies the effect of temperature variation during airflow measurement. The independent parameters such as curve-fitting error in the calibration, A/D resolution uncertainty and probe positioning are also considered in the uncertainty analysis. The uncertainty of the Turbulence Intensity (TI) was found to be around 6%.

3.0 RESULTS

Both time-averaged and time-dependent measurements were acquired in order to determine the steady and unsteady features in the flowfield of an aerofoil with a horn ice shape.

3.1 Time-averaged measurements

The effect of the simulated ice accretion on the aerofoil flowfield will be discussed first by fluorescent oil flow visualisation technique and time-average pressure measurements to provide a better understanding of the integrated results that will be shown later. Figure 4 shows the result of the fluorescent oil flow visualisation at $\alpha = 0°$ and $Re = 1.0 \times 10^6$. The $k/c = 0.0433$ simulated ice shape is located at $s/c = 0.034$. Use of fluorescent oil flow visualisation technique allows for the identification of key features in the time-averaged flowfield, including regions of separated flow and mean shear-layer reattachment location. The time-averaged reattachment location was estimated using the flow bifurcation that occurs at shear-layer reattachment (Fig. 4(a)). As a result of the flow bifurcation, the oil streaks upstream of the reattachment location are scrubbed upstream and the oil streaks downstream of the reattachment location are scrubbed downstream. The speckled region in Fig. 4(b) indicates the mean reattachment zone of the separation bubble, which ranges from $x/c = 0.2$ to $x/c = 0.3$. Upstream of this location inside the separation bubble is a region of reverse

https://doi.org/10.1017/aer.2016.29 Published online by Cambridge University Press

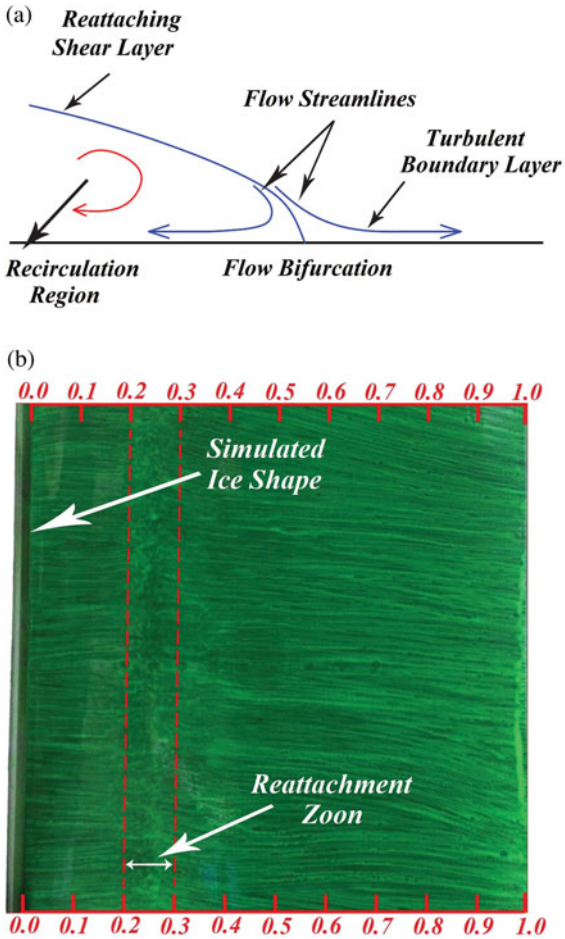

Figure 4. (Colour online) (a) Schematic of shear-layer reattachment on aerofoil surface, after Ansell and Bragg[27], (b) fluorescent oil flow visualisation ($\alpha = 0°$ and $Re = 1.0 \times 10^6$).

flow, indicated by the oil streaks flowing from right to left and downstream, where the flow has reattached as a turbulent boundary layer and moves toward the trailing-edge.

Figure 5 shows the surface pressure distribution on the upper surface of aerofoil with $k/c = 0.0433$ ice shape simulation that is placed at various chord-wise locations (between $s/c = 0$ and 0.034) at $\alpha = 0°$ and is compared with the clean aerofoil. The surface pressure was not measured over the simulated ice shape. Thus the C_p from the last pressure tap upstream of the simulated ice shape is connected to the first pressure tap downstream of the simulated ice shape by a straight line. It is important to note that the shear-layer reattachment location can be approximated by the location where the iced-aerofoil pressure distribution intersects the clean aerofoil one[3,28].

When the simulated ice shape is located at the leading-edge of aerofoil ($s/c = 0$) the pressure distribution appears approximately identical to that of the clean case. In fact, the separation bubble is so small that it is nearly undetectable through pressure distribution comparisons. In Fig. 5 the pressure distribution significantly changes when the simulated ice

https://doi.org/10.1017/aer.2016.29 Published online by Cambridge University Press

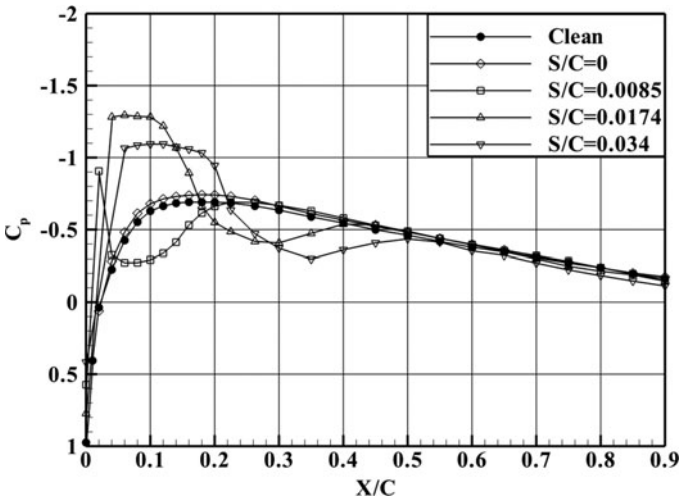

Figure 5. Effect of k/c = 0.0433 simulated ice shape location on a NACA 0015 aerofoil pressure distribution ($\alpha = 0°$ and $Re = 1.0 \times 10^6$).

shape is located at s/c = 0.0085. The pressure distribution shows a suction peak ($C_p = -0.91$) immediately downstream of simulated ice shape as the flow accelerates over it and separates. The pressure coefficients then increases as the reattachment process begins and the shear-layer reattachment location occurs where the iced-aerofoil pressure coefficients approach the clean value at x/c = 0.036. The extremely small bubble is due to the very favourable pressure gradient in which the simulated ice shape is located and the bubble is quickly able to reattach. As the simulated ice shape is moved downstream from the leading edge to s/c = 0.0174, initially the pressure coefficients decreases sharply, indicating the acceleration of flow due to the separation of shear layer from the tip of the ice shape. Pressure recovery is delayed from x/c = 0.04 to x/c = 0.12, resulting in a constant pressure plateau until the shear-layer transitions to turbulent flow[5,6]. Entrainment of high-energy external flow by the turbulent shear layer allows for adequate pressure recovery and results in flow reattachment. After transition, pressure recovery in the separation bubble begins and the reattachment occurs at x/c = 0.18.

Based on Fig. 6, similar trends in the pressure distribution are observed at $\alpha = 4°$, although estimates of shear-layer reattachment location from surface pressures indicate that as the angle-of-attack increases, the bubble length increases as well.

At $\alpha = 4°$, the pressure distribution for the upper surface of clean aerofoil shows a suction peak (with $C_{p,min} = -1.52$) near x/c = 0.03, followed by a severe pressure recovery region (with an adverse pressure gradient). When the simulated ice shape is placed at s/c = 0.0174, the resulting separation bubble would be located in a very adverse pressure gradient where it cannot easily reattach. Thus, the separation bubble for this simulated ice shape location is much larger than when the simulated ice shape is located at s/c = 0.0085. It is interesting to note that when the simulated ice shape is located in the critical location of s/c = 0.0174, the separation bubble eliminates the large leading-edge suction peak of the clean aerofoil. By locating the ice shape at s/c = 0.034, a very long separation bubble will be formed downstream of the ice shape. In this case, both the simulated ice shape and the separation bubble are located in the clean aerofoil adverse pressure gradient region. The effect of a

https://doi.org/10.1017/aer.2016.29 Published online by Cambridge University Press

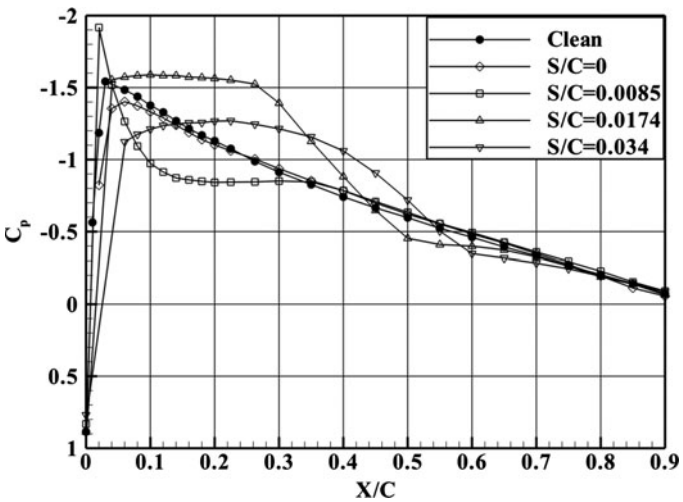

Figure 6. Effect of k/c = 0.0433 simulated ice shape location on a NACA0015 aerofoil pressure distribution ($\alpha = 4°$ and $Re = 1.0 \times 10^6$).

growth in the separation bubble size is associated with a further decrease in the magnitude of the clean aerofoil leading-edge suction peak and a longer length of constant pressure across the aerofoil upper surface. In this situation, determining the reattachment location from the surface pressure distribution is difficult and it is unclear whether or not the separation bubble has reattached.

Figure 7 indicates the effect of height and location of ice shape on the bubble reattachment location at $Re = 1.0 \times 10^6$, based on the surface pressure distribution. The uncertainty of the time-averaged shear-layer reattachment location was determined from the distance between the pressure taps. The maximum uncertainty in the value of reattachment location was 5%. It can be seen that the bubble length is a function of aerofoil angle-of-attack, the height and the location of ice shape. When the $k/c = 0.042$ ice shape is located near the leading edge ($s/c = 0.0085$), the separation bubble remains very small and does not grow significantly with angle-of-attack (Fig. 7(a)). As the $k/c = 0.02$ ice shape is moved downstream from $s/c = 0.0085$ to 0.0174, the growth rate of bubble length increases, although it is not considerable until $\alpha = 4^o$. By increasing the angle-of-attack to $\alpha = 5°$ a dramatic growth in bubble length is observed and the bubble approximately doubles in size from $\alpha = 5°$ to 7°. Figure 7(a) shows a considerable increase in bubble length by moving the $k/c = 0.02$ ice shape to $s/c = 0.034$. The bubble formed at α=0° is eight times longer than the one formed downstream of simulated ice shape located at $s/c = 0.0085$. With an increasing angle-of-attack, the bubble length grows sharply from $x/c = 0.16$ at $\alpha = 0°$ to $x/c = 0.40$ at $\alpha = 4°$.

When $k/c = 0.0433$ simulated ice shape is placed at $s/c = 0.0085$ (Fig. 7(b)), the variations of ice height don't cause any appreciable change in reattachment location because the bubble is able to attach quickly in the very favourable pressure gradient. Figure 7 reveals that as the simulated-ice shape is moved downstream from the leading edge to $s/c = 0.0174$ and $s/c = 0.034$, the differences in the ice shape height have a progressively larger effect on the reattachment location. For example, when the simulated ice shape is located at $s/c = 0.0174$ ($\alpha = 0$), increasing the ice shape height from $k/c = 0.02$ to $k/c = 0.0433$ approximately quadruples the bubble length.

https://doi.org/10.1017/aer.2016.29 Published online by Cambridge University Press

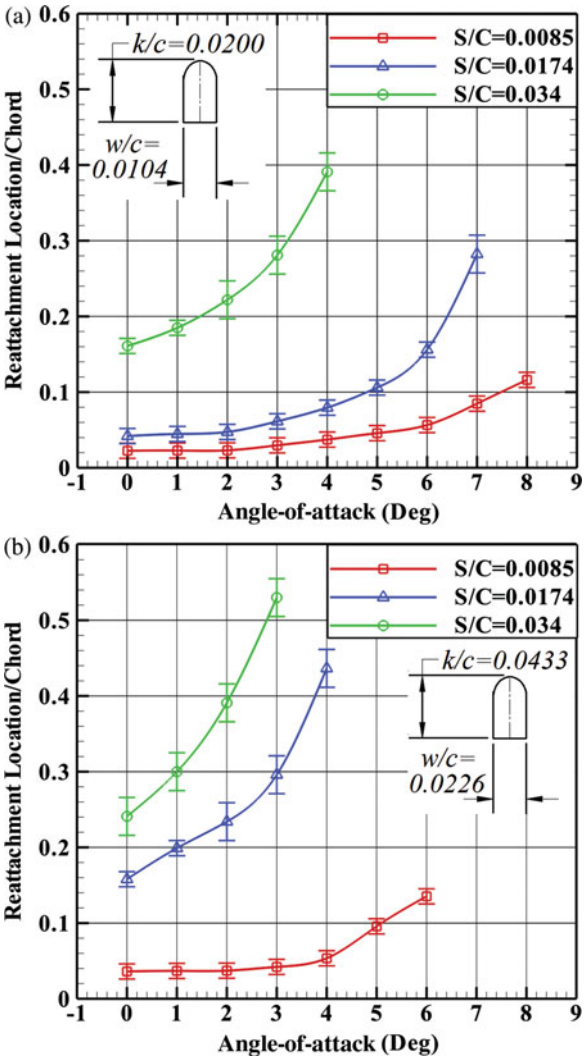

Figure 7. (Colour online) Time-averaged shear-layer reattachment location with (a) k/c = 0.02 simulated ice shape and (b) k/c = 0.0433 simulated ice shape (Re = 1.0×10^6).

3.2 Ice-induced flowfield unsteadiness

Figure 8 presents a comparison between the time-average surface pressure distribution and the variation of root-mean-square pressure fluctuations (C_p') for the upper surface of iced-aerofoil at $\alpha = 0°$ (k/c = 0.0433 and s/c = 0.034). In Fig. 8 the reattachment region is marked with purple and yellow colours, and the location where the maximum C_p' occurs is marked with blue and yellow colours. The yellow colour has been used to mark the area where an overlap of maximum C_p' and reattachment position is seen. This minor overlap between the location of maximum C_p' and reattachment region only occurs at low angles of attack. It's shown that as the flow approaches the simulated ice shape and the separation region, the RMS pressure fluctuations begins to increase. The highest value of RMS pressure fluctuations is observed

https://doi.org/10.1017/aer.2016.29 Published online by Cambridge University Press

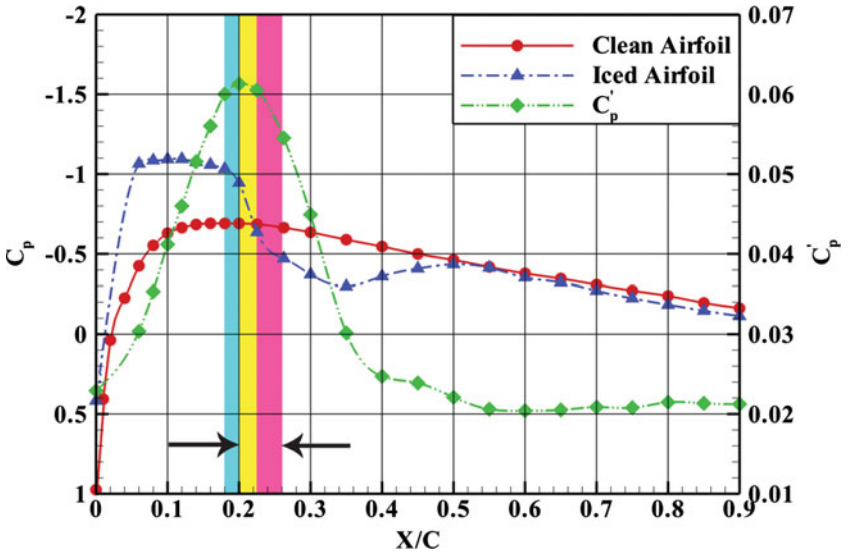

Figure 8. (Colour online) Distribution of C_p and C_p' for a NACA 0015 aerofoil with simulated horn-ice shape ($\alpha = 0°$, Re $= 1.0 \times 10^6$, k/c $= 0.0433$ and s/c $= 0.034$).

upstream of reattachment location. This phenomenon is due to roll-up of vortices immediately originated from the separation edge and shedding of the large-scale vortex structures. Vortex shedding causes high velocity fluctuations, and in turn, high pressure fluctuations in the reattachment region. Downstream of the reattachment, the RM values of pressure fluctuations begin to decay due to the boundary layer relaxation process following reattachment region and settle down to the smooth surface values.

Similar observations were reported by Gurbacki[29], who stated that immediately downstream of the ice horn, the RMS fluctuations in C_p are small—only slightly above those measured for the clean aerofoil at the same chord-wise position. However, C_p' increased rapidly with increasing chord-wise position, reaching a maximum value of 0.10 just upstream of the reattachment zone. Moreover, in an attempt to measure the wall pressure fluctuations for a backward-facing step by Feng et al[30], a maximum of RMS surface pressure was detected near the reattachment point, which confirms the above mentioned distribution of C_p'. A comparison of the locations of maximum C_p' and time-averaged reattachment location are shown in Fig. 9 (k/c $= 0.0433$ and s/c $= 0.0174$). It can be seen that the location of maximum unsteadiness in the flowfield corresponding to the location of maximum C_p' does not exactly correspond to the location of mean shear-layer reattachment. Furthermore with increasing angle-of-attack, the location of maximum C_p' tends to reside farther upstream of the reattachment location. For the angle-of-attack range included in Fig. 9, the location of maximum C_p' occurs between $x/x_{MR} = 0.67$ and $x/x_{MR} = 0.9$.

At an angle-of-attack range from $\alpha = 0°$ to 5°, Gurbacki[29] identified the maximum unsteadiness in surface pressure occurring between $x/x_{MR} = 0.60$ and $x/x_{MR} = 0.75$. As discussed by Mabey[31], the location of maximum fluctuation in pressure on a surface with reattaching flows typically resides between $x/x_{MR} = 0.75$ and $x/x_{MR} = 0.90$, which confirms the results of the current study. Moreover, Heenan and Morrison[32] observed that the location of maximum unsteadiness in the surface pressure downstream of a backward-facing step resided between $x/x_{MR} = 0.8$ and $x/x_{MR} = 0.90$.

https://doi.org/10.1017/aer.2016.29 Published online by Cambridge University Press

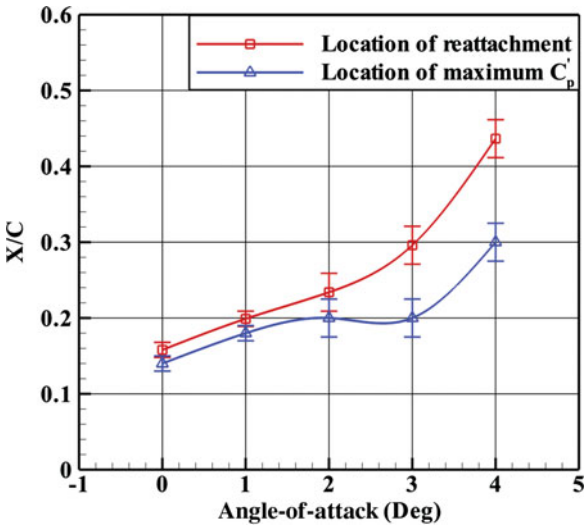

Figure 9. (Colour online) Comparison of chord-wise location of mean reattachment and maximum C_p' (Re = 1.0 × 10^6).

Figure 10 shows the effect of height and location of ice shape on distribution of C_p'. The simulated ice shape is located at s/c = 0.0085, 0.00174 and 0.034. It can be seen that the maximum value of C_p' increases when the simulated ice shape is moved from s/c = 0.0085 to s/c = 0.034. It can be also observed that with increasing the height of the ice shape (for a fixed angle-of-attack), the value of maximum C_p' generally increases and the corresponding location of this maximum value moves downstream.

The upper surface distribution of C_p' at various angles of attack for the NACA 0015 aerofoil with simulated ice shape is shown in Fig. 11 (k/c = 0.0433 and s/c = 0.034). At low angles of attack ($\alpha = 0°$ and 1°), the elevated levels of unsteadiness are primarily constrained to the leading-edge section of the aerofoil from approximately x/c = 0.1 to x/c = 0.3. With increasing the angles of attack to $\alpha = 2°$ and 3°, the maximum value of C_p' reached across the upper surface increases and moves further downstream. As seen in Fig. 11(b) for $\alpha = 4°$ and 5°, the unsteadiness in the leading-edge region from x/c = 0.0 to x/c = 0.3 begins to increase. An increase in angle-of-attack to 6° and 7° reveals that the value of maximum C_p' begins to decrease and the distribution of unsteadiness across the aerofoil flowfield moves closer to being uniform. The trends in the flowfield unsteadiness are qualitatively consistent with the observations of Ansell[33], who reported increasing in the flowfield unsteadiness with angle-of-attack until stall. This author also stated that flowfield unsteadiness decreased when the angle-of-attack was increased past stall.

3.3 Regular mode of vortical motion

In addition to estimating the distribution of unsteadiness across the aerofoil surface using the calculated C_p' values, it is also helpful to identify frequency scales associated with the unsteadiness. As mentioned before one of the sources of unsteadiness present in most separated flows is due to vortices that form in the shear-layer and vortex shedding downstream of the reattachment location in regular frequencies. According to the general trends of the upper surface velocity spectra, the iced aerofoil flowfield unsteadiness associated with the vortices frequency was examined in the velocity spectra at the nearest point to the

https://doi.org/10.1017/aer.2016.29 Published online by Cambridge University Press

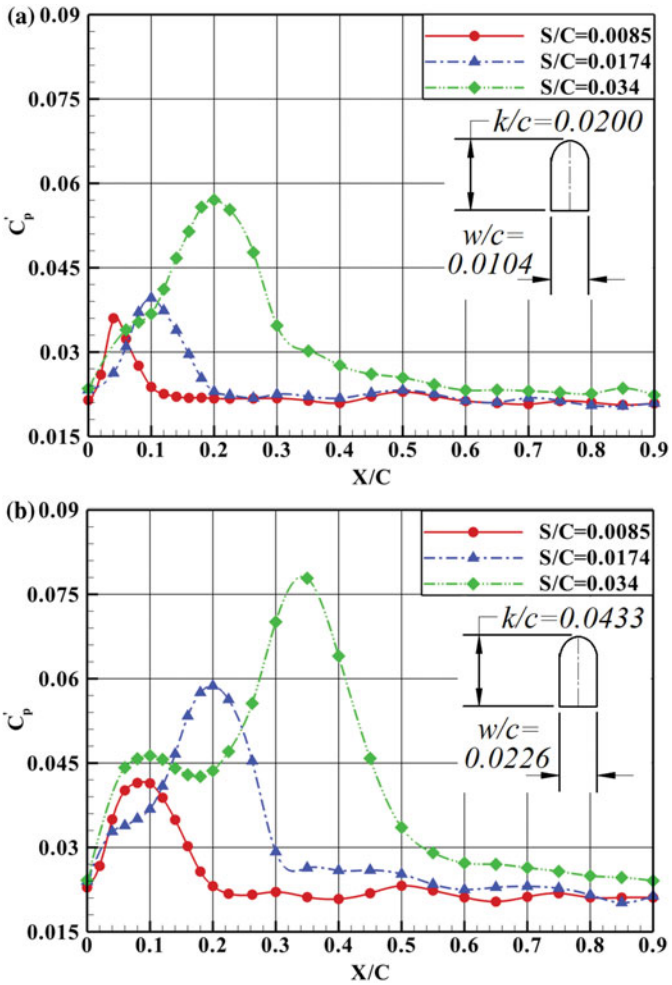

Figure 10. (Colour online) Effect of simulated ice shape location on C_p': (a) k/c = 0.02, (b) k/c = 0.0433 ($\alpha = 2°$ and Re = 1.0×10^6).

reattachment location[10]. Near the reattachment region, the vortex structures are well defined and close to the aerofoil surface, and therefore are easily sensed by the hot-wire probe.

Figure 12 shows the regular frequency of the vortices motion in the shear-layer of the iced-aerofoil (k/c = 0.0433 and s/c = 0.034) at Reynolds number of 1.0×10^6 and angles of attack of $\alpha = 0°$, 1°, 2° and 3°. The central frequency of the local maximum spectrum amplitude corresponds to the regular frequency of the vortices.

It is seen that the bandwidth and central frequency of the regular mode spectral peaks decrease with increasing the angle-of-attack. At $\alpha = 0°$, energy in the low frequency range decreases somewhat near 50 Hz, after which the amplitudes increase slightly to a local maximum that is centred near the frequency of 220 Hz. An increase in angle-of-attack to 1° and 2° reveals a local maximum amplitude at 175 Hz and 135 Hz, respectively. Finally, at a = 3°, the regular frequency occurs at 125 Hz. It can also be observed from Fig. 12 that the amplitude of the regular mode spectral peak increases with increasing the

https://doi.org/10.1017/aer.2016.29 Published online by Cambridge University Press

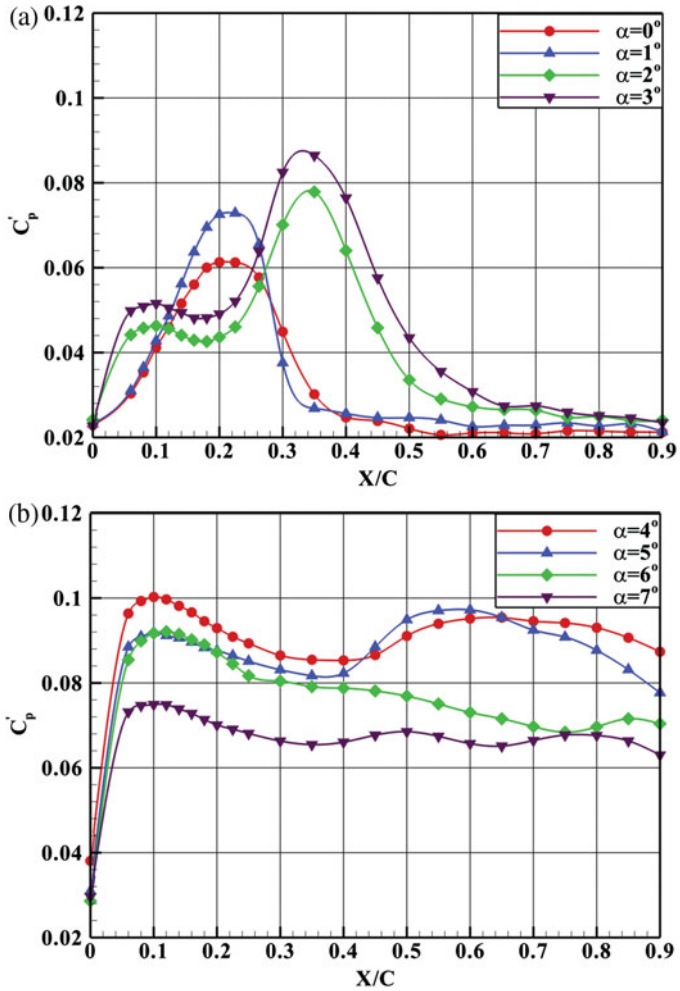

Figure 11. (Colour online) Distribution of C_p' for a NACA 0015 aerofoil with k/c = 0.0433 simulated horn-ice shape (s/c = 0.034): (a) angle-of-attack range from 0° to 3°, (b) angle-of-attack range from 4° to 7°.

angle-of-attack. This phenomenon indicates that as the adverse pressure gradient imposed across the separation region increases and as the separation bubble elongates, the oscillations imposed by vortical motion become more energetic.

A comparison of the Strouhal number values for the regular mode from the current study were made with values reported in the literature. This comparison is presented in Table 1. The Strouhal number $St_r = fL_R/V$ is calculated for each case based on the length of the separation bubble (L_R) and the freestream velocity (V). These values range from 0.5 to 0.63 and are in good agreement with those of other separated flow fields reported in Refs 10-12 and 14.

Figure 13 shows the regular frequency of the vortices downstream of the reattachment location at $\alpha = 3°$ and $Re = 1.0\times10^6$ (k/c = 0.0433, s/c = 0.034). These frequencies were captured with hot-wire anemometry normal to the chord-wise direction where the turbulence intensity is maximum. Figure 13 reveals a decrease in the regular mode frequency, with

https://doi.org/10.1017/aer.2016.29 Published online by Cambridge University Press

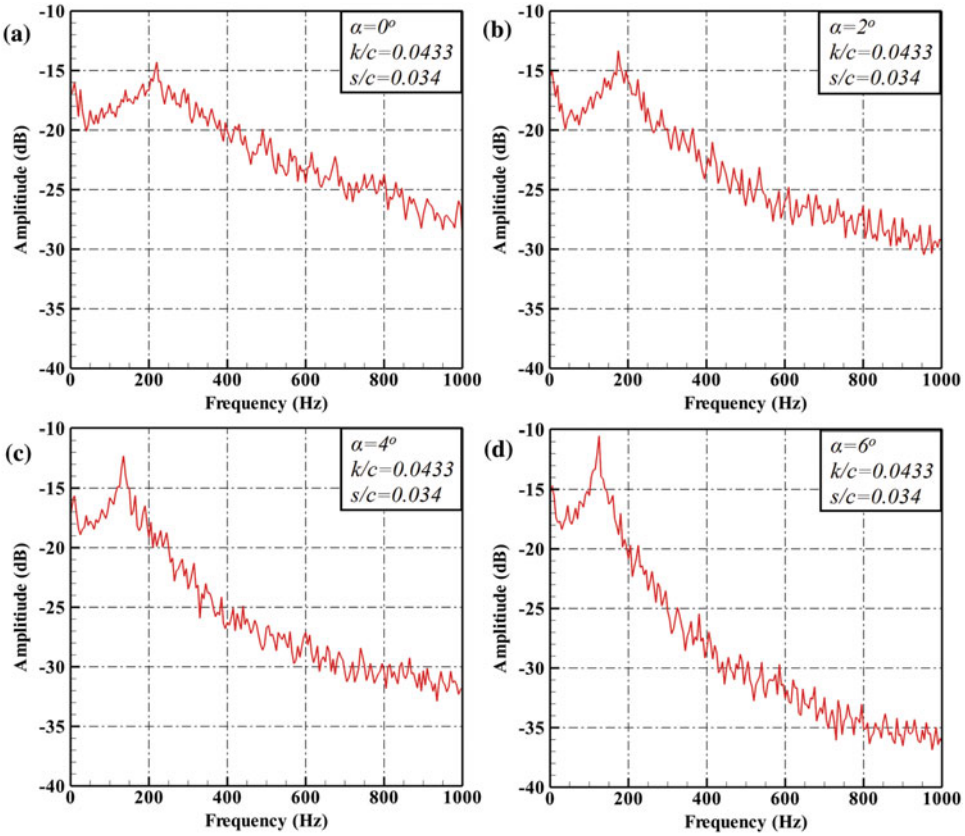

Figure 12. (Colour online) Regular vortex frequency: power spectral density function of the time-dependent velocity fluctuation near reattachment location ($Re = 1.0 \times 10^6$, $k/c = 0.0433$, $s/c = 0.034$). (a) $\alpha = 0°$, (b) $\alpha = 1°$, (c) $\alpha = 2°$, (d) $\alpha = 3°$.

increasing distance downstream of the reattachment location. It can also be seen in Fig. 13 that the frequency of the regular mode remains unchanged from $x/x_{MR} = 1.7$ to $x/x_{MR} = 1.9$. Similar trends were observed at other angles of attacks. These data are in good agreement with the results of Cherry et al[11] who reported decreasing in the regular mode frequency of the pressure spectrum downstream of a backward facing step. They attributed the decrease in frequency to changes in the shear-layer structure that occur upstream of the reattachment zone, until a constant shedding frequency is reached.

3.4 Shear-layer flapping

As discussed before, the shear-layer flapping phenomenon is a low frequency source of unsteadiness associated with separation bubbles that is characterised by a vertical 'flapping' motion of the shear layer and a stream-wise oscillation of the shear-layer reattachment location. The effects of the shear-layer flapping phenomenon on the iced-aerofoil wake velocities of the aerofoil could be observed downstream of the aerofoil upper surface. As the separation bubble underwent a quasi-periodic surface-normal flapping, the streamlines just above the separation bubble were forced to oscillate with the flapping motion. This motion

https://doi.org/10.1017/aer.2016.29 Published online by Cambridge University Press

Table 1
Comparison of St_r for regular mode determined in the current study with those reported in the literature

Author(s)	Geometry	Reynolds Number	Strouhal Number (fL/V)
Current study	NACA 0015 aerofoil (with 2D horn-ice shape)	$Re = 1 \times 10^6$	0.5-0.63
Gurbacki[4]	NACA 0012 aerofoil (with 2D and 3D horn-ice shape)	$Re = 1.0 \times 10^6$-1.8×10^6	0.53-0.73
Mirzaei et al[10]	NLF-0414 aerofoil (with 2D horn-ice shape)	$Re = 0.5 \times 10^6$	0.44-0.78
Cherry et al[11]	2D blunt flat plate	$Re = 3.2 \times 10^4$	0.7
Driver et al[12]	2D backward-facing step	$Re = 3.7 \times 10^4$	0.6
Kiya and Sasaki[14]	2D blunt flat plate	$Re = 2.6 \times 10^4$	0.6

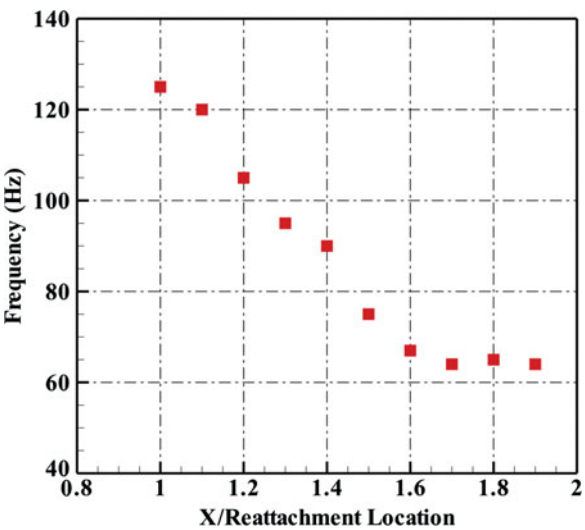

Figure 13. (Colour online) Vortex frequency distribution downstream of the reattachment location ($\alpha = 3°$ and $Re = 1.0 \times 10^6$, $k/c = 0.0433$, $s/c = 0.034$).

then cause the streamlines to sweep across the hot-wire probe in the wake downstream of the separation bubble according to the flapping frequency. An example of the shear-layer flapping mode in wake velocity spectra is shown in Fig. 14 for the iced aerofoil ($k/c = 0.02$ and $s/c = 0.0174$) at Reynolds number of 1.0×10^6 and angles of attack of $\alpha = 6°$ and 7°. Since the shear-layer flapping phenomenon has been observed to affect the entire separation bubble, its effects in the wake could be seen across the entire upper-surface wake region. Anyway, the shear-layer flapping mode were measured at $x/c = 1.45$ and $y/c = 0.16$. It should be stressed that these low-frequency oscillations are not attributed to any instabilities induced

https://doi.org/10.1017/aer.2016.29 Published online by Cambridge University Press

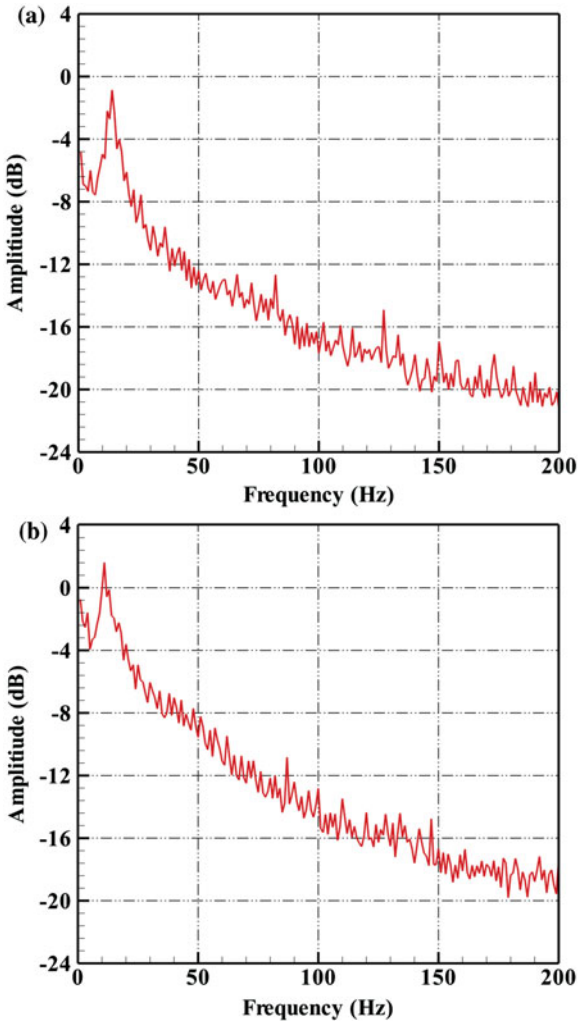

Figure 14. (Colour online) Frequency of shear-layer flapping mode ($Re = 1.0 \times 10^6$, $k/c = 0.02$, $s/c = 0.0174$), (a) $\alpha = 6°$, (b) $\alpha = 7°$.

by the wind-tunnel fan. The frequencies of fan blade passing were identified as occurring at frequencies much higher than those observed for the shear-layer flapping mode.

Strouhal numbers based on the aerofoil projected height and the freestream velocity are calculated for the peak frequencies identified in wake velocity spectra (St_f). The Strouhal numbers associated with this shear-layer flapping mode correspond to $St_f = 0.0210$ and 0.0186. The values of Strouhal numbers of the shear-layer flapping mode are compared with those reported in the literature. A summary of this comparison is presented in Table 2.

From Table 2, the values of St_f for shear-layer flapping obtained in the current study are consistent with the range of values reported in the literature. This suggests that the low-frequency peak that is identified in the current study with central frequency between 11 Hz and 13 Hz can be attributed to the same shear-layer flapping mechanism observed in separation bubble flowfields about iced aerofoils and simple geometries.

https://doi.org/10.1017/aer.2016.29 Published online by Cambridge University Press

Table 2
Comparison of St_f for shear-layer flapping determined in the current study with those reported in the literature

Author(s)	Geometry	Reynolds Number	Strouhal Number (f(c × sine α)/V)
Current Study	NACA 0015 aerofoil (with 2D horn-ice shape)	$Re = 1 \times 10^6$	0.0186-0.021
Zaman and Potapczuk[18]	NACA 0012 aerofoil (with 2D glaze-ice)	$Re = 0.75 \times 10^5$-1.25×10^6	0.0153
Bragg et al[3]	NACA 0012 aerofoil (with 2D glaze-ice)	$Re = 1.5 \times 10^6$	0.0185
Cherry et al[11]	2D blunt flat plate	$Re = 3.2 \times 10^4$	0.033
Driver et al[12]	2D backward-facing step	$Re = 3.7 \times 10^4$	0.012
Kiya and Sasaki[14]	2D blunt flat plate	$Re = 2.6 \times 10^4$	<0.025

3.5 Turbulence intensity

The turbulence intensity contours for the separated shear-layer regions were found to be in agreement with results from other separated flows. In this case, the turbulence intensity was calculated as the root mean square of the fluctuating stream-wise velocity and normalised by the freestream velocity. An example of these data is shown in Fig. 15 for the iced aerofoil at $\alpha = 3°$ and 6° ($k/c = 0.0433$ and $s/c = 0.034$). The separated shear-layer is visible in RMS stream-wise velocity as the region where large fluctuations are observed[28]. As shown in Fig. 15(a), a region with high velocity fluctuation in the range of 23%-28% in the middle of the separated shear layer in the vicinity of reattachment location is evident (the reattachment location is marked with a dashed line). This region of peak turbulence intensity begins downstream of $x/c = 0.3$, which has been identified as the location of maximum unsteadiness from the pressure data (Fig. 11(a)).

With increasing the angle-of-attack to 6° (Fig. 15(b)), the separation bubble fails to reattach; consequently, the flowfield separates completely. It is interesting to note that at $\alpha = 3°$ downstream of the reattachment location, the turbulence intensity levels decrease gradually, but at $\alpha = 6°$, this high turbulence intensity region extends to downstream of trailing edge and the decay of maximum turbulent intensity cannot be seen until $x/c = 1.2$.

4.0 CONCLUSION

The main purpose of this investigation was to identify the dominant sources of unsteadiness in the flowfield of the separation bubble formed on a NACA 0015 aerofoil with glaze ice accretion. The unsteady flow features were determined using measurements of the time-dependent aerofoil surface pressure distribution and spectral analysis of stream-wise velocity fluctuations at a Reynolds number of 1.0×10^6. The maximum amount of unsteadiness (C_p') in the iced-aerofoil flowfield consistently resided upstream of the mean shear-layer reattachment location. In this study, the average location of maximum flowfield unsteadiness was determined at $x/x_{MR} = 0.8$. Furthermore, spectral analysis of the stream-wise velocity

https://doi.org/10.1017/aer.2016.29 Published online by Cambridge University Press

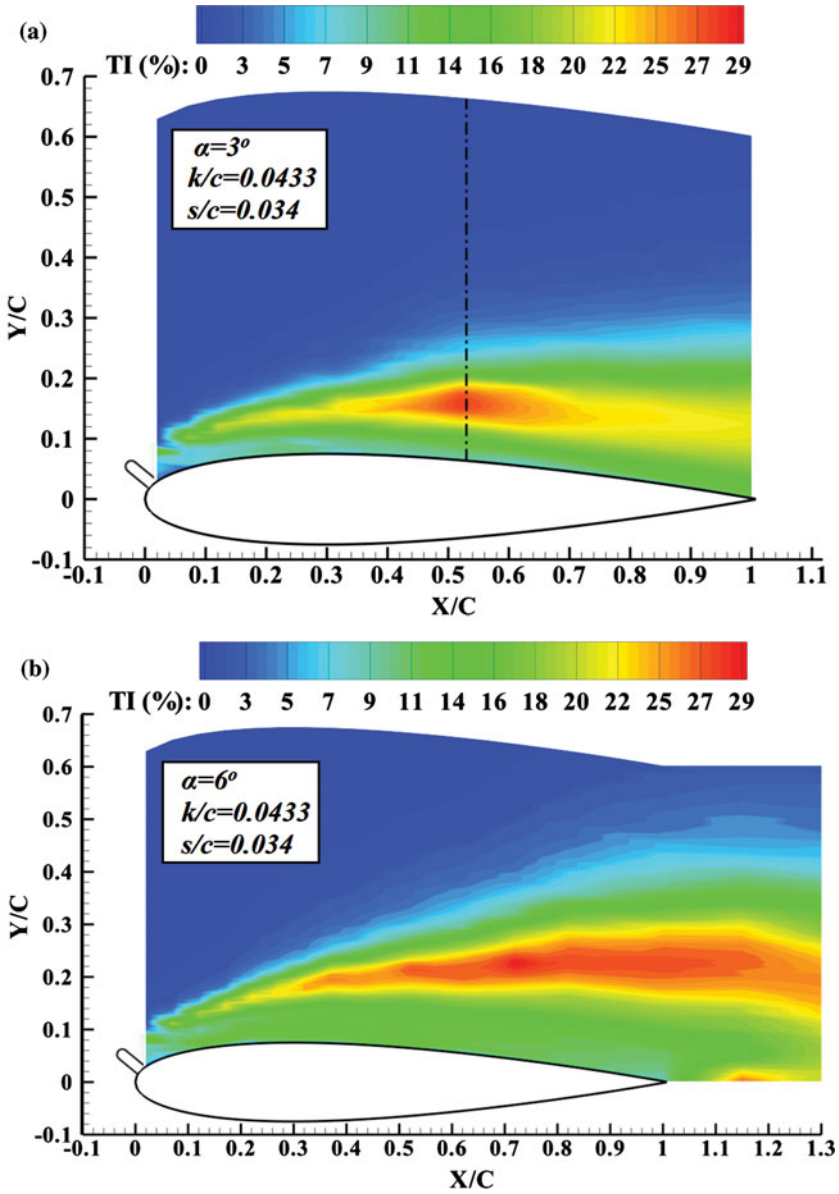

Figure 15. (Colour online) Contour of turbulence intensity, (a) $\alpha = 3°$, (b) $\alpha = 6°$ ($Re = 1.0 \times 10^6$, $k/c = 0.0433$, $s/c = 0.034$).

fluctuations confirmed the existence of the two distinct sources of unsteadiness in the iced-aerofoil flowfield including the regular mode of vortical motion and the shear-layer flapping mode. The regular mode was attributed to flowfield unsteadiness due to vortical motion in the separated shear-layer and vortex pairing and shedding from the separation bubble. The centre frequency of the regular mode typically occurred between 220 Hz and 125 Hz. The effects of shear-layer flapping were observed across a narrow-band, low-frequency range. The centre frequency of the shear-layer flapping mode typically occurred between 11 Hz and 13 Hz.

https://doi.org/10.1017/aer.2016.29 Published online by Cambridge University Press

REFERENCES

1. BUSCH, G., BROEREN, A.P. and BRAGG, M.B. Aerodynamic simulation of a horn-ice accretion on a subscale model, *J Aircr*, 2008, **45**, (2), pp 604-613.
2. LYNCH, F. and KHODADOUST, A. Effects of ice accretions on aircraft aerodynamics, *Progress in Aerospace Sciences*, 2001, **37**, pp 669-767.
3. BRAGG, M.B., KHODADOUST, A. and SPRING, S.A. Measurements in a leading-edge separation bubble due to a simulated airfoil ice accretion, *AIAA J*, 1986, **30**, (6), pp 1462-1467.
4. GURBAKI, H.M. and BRAGG, M.B. Unsteady flowfield about an iced airfoil, 42th AIAA Aerospace Sciences Meeting & Exhibit, 5-8 January 2004, Reno, Nevada, US.
5. JACOBS, J.J. and BRAGG, M.B. Two- and three-dimensional iced airfoil separation bubble measurements by particle image velocimetry, 45th AIAA Aerospace Sciences Meeting & Exhibit, 8-11 January, Reno, Nevada, US.
6. JACOBS, J.J. and BRAGG, M.B. Particle image velocimetry measurements of the separation bubble on an iced airfoil, 24th AIAA Applied Aerodynamics Conference, 5-8 June 2006, San Francisco, California, US, 2006.
7. DECK, S. and THORIGNY, P. Unsteadiness of an axisymmetric separating-reattaching flow: Numerical investigation, *J Physics of Fluids*, 2007, **19**, 065103.
8. SIGURDSON, L.W. The structure and control of a turbulent reattaching flow, *J Fluid Mechanics*, 1995, **298**, pp 139-165.
9. KIYA, M.S., SHIMIZU, M. and MOCHIZUKI, O. Sinusoidal forcing of a turbulent separation bubble, *J Fluid Mechanics*, 1997, **342**, pp 119-139.
10. MIRZAEIA, M. ARDEKANI, M.A. and DOOSTTALAB, M. Numerical and experimental study of flow field characteristics of an iced airfoil, *J Aerospace Science and Technology*, 2009, **13**, pp 267-276.
11. CHERRY, N.J., HILLIER, R. and LATOUR, M.E.M.P. Unsteady measurements in a separated and reattaching flow, *J Fluid Mechanics*, 1984, **144**, pp 13-46.
12. DRIVER, D.M., SEEGMILLER, H.L. and MARVIN, J.G. Time-dependent behavior of a reattaching shear layer, *AIAA J*, 1987, **25**, (7), pp 914-919.
13. EATON, J.K. and JOHNSTON, J.P. Low frequency unsteadiness of a reattaching turbulent shear layer, Turbulent Shear Flows III, Third International Symposium on Turbulent Shear Flows, September 1981, University of California at Davis, US, pp 162-170.
14. KIYA, M. and SASAKI, K. Structure of a turbulent separation bubble, *J Fluid Mechanics*, 1983, **137**, pp 83-113.
15. KIYA, M. SHIMIZU, M. and MOCHIZUKI, O. Sinusoidal forcing of a turbulent separation bubble. *J Fluid Mechanics*, 1997, **342**, pp 119-139.
16. LEE, I. and SUNG, H.J. Multiple-arrayed pressure measurement for investigation of the unsteady flow structure of a reattaching shear layer, *J Fluid Mechanics*, 2002, **463**, pp 377-402.
17. SIGURDSON, L.W. The structure and control of a turbulent reattaching flow, *J Fluid Mechanics, September* 1995, **298**, pp 139-165.
18. ZAMAN, K.B.M.Q. and POTAPCZUK, M.G. The low-frequency oscillation in the flow over a NACA 0012 airfoil with an 'iced' leading edge, NASA/TM-102018, June 1989.
19. BRAGG, M.B., BROEREN, A.P. and BLUMENTHAL, L.A. Iced-airfoil aerodynamics, *Journal of Progress in Aerospace Sciences*, 2005, **41**, pp 323-362.
20. HAROLD, E. and ADDY, J.R. Ice accretions and icing effects for modern airfoils, NASA Technical Reports Server, NASA/TP 2000-210031, April 2000.
21. LEE, S. and BRAGG, M.B. Investigation of factors affecting iced-airfoil aerodynamics, *J Aircraft*, 2003, **40**, (3), pp 499-508.
22. BYNUM, D.S., LEDFORD, R.L. and SMOTHERMAN, W.E. Wind tunnel pressure measuring techniques, AEDC-TR-70-250, 1970.
23. BARLOW, J.B., WILLIAM, H.R. and POPE, A. *Low-Speed Wind Tunnel Testing*, 3rd ed, 1999, John Wiley & Sons, New York, NY, US.
24. SOLTANI, M.R., RASI, F., SEDDIGHI, M. and BAKHSHALIPOUR, A. An experimental investigation of time lag in pressure-measuring systems, 2nd Ankara International Aerospace Conference, AIAC-2005-028, August 2005.
25. JORGENSON, F. *How to Measure Turbulence with Hot-wire Anemometers (A Practical Guide)*, 2002, Dantec Dynamics, Skovlunde, Denmark.

https://doi.org/10.1017/aer.2016.29 Published online by Cambridge University Press

26. YAVUZKURT, S. A guide to uncertainty analysis of hot-wire data, *J Fluids Engineering*, Jun 1984, **106**, pp 181-186.
27. ANSELL, P.J. and BRAGG, M.B. Measurement of unsteady flow reattachment on an airfoil with a leading-edge horn-ice shape, 30th AIAA Applied Aerodynamics Conference, 25-28 June 2012, New Orleans, Louisiana, US.
28. BROEREN, A.P. and BRAGG, M.B. Flowfield measurements about an airfoil with leading edge ice shapes, *J Aircr*, 2006, **43**, (4), pp 1226-1243.
29. GURBAKI, H.M. Ice-Induced Unsteady Flowfield Effects on Airfoil Performance, Ph.D. Dissertation, University of Illinois at Urbana-Champaign, US, 2003.
30. FENG, K.E., YING ZHENG, L.I.U. and HAN-PING, C.H.E.N. Simultaneous flow visualisation and wall-pressure measurement of the turbulent separated and reattachment flow over a backward facing step, *J Hydrodynamics*, 2007, **19**, (2), pp 180-187.
31. MABEY, D.G. Analysis and correlation of data on pressure fluctuations in separated flow, *J Aircr*, 1972, **9**, (9), pp 642-645.
32. HEENAN, A.F. and MORRISON, J.F. Passive control of pressure fluctuations generated by separated flow, *AIAA J*, 1998, **36**, (6), pp 1014-1022.
33. ANSELL, P.J. Unsteady Modes in the Flowfield About an Airfoil with a Leading-Edge Horn-Ice Shape, 2013, Ph.D. Dissertation, University of Illinois at Urbana-Champaign, US.

https://doi.org/10.1017/aer.2016.29 Published online by Cambridge University Press